

Growth mechanisms of perturbations in boundary layers over a compliant wall

M. Malik¹, Martin Skote², and Roland Bouffanais^{1*}

¹*Singapore University of Technology and Design,*

²*School of Mechanical and Aerospace Engineering, Nanyang Technological University, Singapore*

(Dated: July 6, 2021)

The temporal modal and nonmodal growth of three-dimensional perturbations in the boundary layer flow over an infinite compliant flat wall is considered. Using a wall-normal velocity/wall-normal vorticity formalism, the dynamic boundary condition at the compliant wall admits a linear dependence on the eigenvalue parameter, as compared to a quadratic one in the canonical formulation of the problem. As a consequence, the continuous spectrum is accurately obtained. This enables us to effectively filter the pseudospectra, which is a prerequisite to the transient growth analysis. An energy-budget analysis for the least-decaying hydroelastic (static-divergence, traveling-wave-flutter and near-stationary transitional) and Tollmien–Schlichting modes in the parameter space reveals the primary routes of energy flow. Moreover, the maximum transient growth rate increases more slowly with the Reynolds number than for the solid wall case. The slowdown is due to a complex dependence of the wall-boundary condition with the Reynolds number, which translates into a transition of the fluid-solid interaction from a two-way to a one-way coupling. Unlike the solid-wall case, viscosity plays a pivotal role in the transient growth. The initial and optimal perturbations are compared with the boundary layer flow over a solid wall; differences and similarities are discussed.

PACS numbers: 47.20.-k, 47.20.Ib

arXiv:1705.02615v2 [physics.flu-dyn] 14 Jan 2018

* Corresponding Author: bouffanais@sutd.edu.sg

I. INTRODUCTION

The interaction between a compliant wall and fluid flow is of high interest among researchers due to their relevance to drag-reduction problems and biofluid mechanics [1, 2]. Such interest arose following the pioneering experiments by [3], and subsequent studies by [4]. Compliant walls also help delay transitions caused by Tollmien–Schlichting waves, which was predicted theoretically [5, 6], and confirmed experimentally [7]. This interaction between compliant wall and flow was theoretically modeled as wall-admittance by [8], while subsequent workers treated it as a two-way coupling, in which the wall is regarded as a membrane with a plate-like behavior that responds through its velocity field to the flow-induced forcing in a typical fashion of fluid-structure interaction [5, 9]. The compliant wall has also been modeled in a more complex way as the upper wall of one or more viscoelastic layers [10].

While the fluid-based Tollmien–Schlichting modes are inhibited by the wall compliance, the elastic nature of the wall gives rise to new modes of instability, namely static-divergence modes and traveling wave flutter, which are collectively known as *hydroelastic modes* [11, 12]. The phase-speed of the traveling wave-flutter is found to be approximately coinciding with the free wave-speed of the wall when neglecting both wall-damping and fluid-forcing. The static divergence mode, has its origin in excessive wall-damping.

Among the three types of modes, the Tollmien–Schlichting and the traveling wave-flutter are prone to convective instability, and can be washed out downstream by the mean flow. However, in the particular case of an infinite compliant wall—when the natural phase-speed of the wall falls within the range of the phase-speed of Tollmien–Schlichting waves, it is hard to distinguish between instabilities due to hydroelastic modes and Tollmien–Schlichting ones as they coalesce to form one single unstable mode in the absolute sense [13–15] such that, if they are present at a certain location, they remain there at all later time, while growing in amplitude and spreading in space. Such different modes and their coalescence can also be identified in a spatial stability calculation of a flow over finite compliant panels. Such mode-coalescence phenomenon has been tracked in the wave-number plane, and its absolutely unstable nature established [16]. This instability due to hydroelastic modes occur at low Reynolds numbers—much smaller than the critical Reynolds number of an otherwise rigid wall, but with a growth rate much smaller than the one of Tollmien–Schlichting waves. Due to the presence of such hydroelastic modes, even at low Reynolds numbers, compliant panels—with streamwise-length optimized between the growing hydroelastic modes and inhibited Tollmien–Schlichting modes—are prescribed for the purpose of drag-reduction [10, 17]. Recently, [18] has studied the global (temporal) traveling-wave-flutter modes in the presence of finite-size compliant panels through a hybrid numerical technique where the temporal eigensystem is provided with an input of spatial eigenvalues from a separate spatial stability calculation. They have also studied the transient growth of a superposition of normal modes.

In this paper, we perform for the first time a transient growth analysis of the problem of hydrodynamic stability of a zero-pressure gradient boundary layer flow over a flat plate with a normal-velocity/normal-vorticity formalism for the study of three-dimensional (3D) modes. This formalism yields a tractable linear-eigenvalue problem without the need to resort to the traditional companion-matrix formulation, hence avoiding an unnecessary increase in the number of unknowns (see e.g., [16, 18–20]). Our new alternative formalism results in the linear appearance of an otherwise quadratic form of the eigenvalue parameter. By means of a specific spectral method formulation for the continuous spectrum, we have access to more accurate members of a superposition-state (i.e. a non-eigenstate) for the first time, which is instrumental in performing the transient growth analysis for this problem. We identify different types of modes and their associated eigenfunctions, such as the static divergence, traveling-wave-flutter and Tollmien–Schlichting modes, and present the unstable regions in the parameter space.

A complete transient-growth study is conducted, which is supplemented with an energy budget analysis of both modal and nonmodal growths. The nonmodal evolution of a state of superposition of modes is analyzed in the plane of wavenumbers. This allows us to identify, for the first time, the optimal perturbation structure associated with maximum transient growth. This analysis of nonmodal evolution is important as it leads to the identification of optimal perturbation structures, which can be anticipated to be present in a bypass transition. To this aim, we follow the traditional method developed by [21] and [22] (See also, [23]).

II. LINEAR PROBLEM FORMULATION AND NUMERICAL APPROACH

Let x , y and z be the streamwise, normal and spanwise directions, respectively, and let $(\hat{u}, \hat{v}, \hat{w})^T$ be the velocity fluctuations to the mean flow $(U_0(y), 0, 0)^T$ in the respective directions, where the mean flow is described under the approximation of parallel flow with $U_0(y)$ obtained from the solution to the Blasius equation (see Fig. 1). We study the flow stability using as variables the fluctuations in normal-velocity, \hat{v} and normal-vorticity $\hat{\eta} \equiv \partial\hat{u}/\partial z - \partial\hat{w}/\partial x$. This has the advantage of reducing the order of the discretized matrix of the resulting eigensystem [23]. Let $\hat{\mathbf{q}} = (\hat{v}, \hat{\eta})^T$, and $\hat{\mathbf{q}} = \mathbf{q}'(y) \exp[i(\alpha x + \beta z - \omega t)]$ where α , β and ω are the streamwise and spanwise wavenumbers, and complex

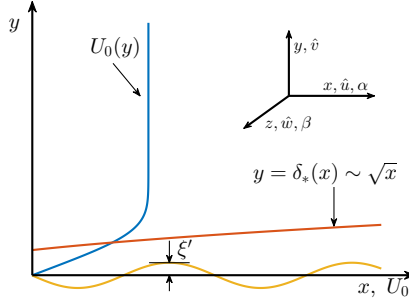


FIG. 1. Schematic diagram: the thick solid line represents the mean-velocity profile with respect to y ; dashed line shows a modal-perturbed compliant wall; dotted line is the displacement-thickness with respect to x .

frequency, respectively. The amplitude \mathbf{q}' is governed by a system of Orr–Sommerfeld (OS) and Squire equations [23]:

$$\begin{pmatrix} A_{11} & 0 \\ \beta D U_0 & A_{22} \end{pmatrix} \begin{pmatrix} v' \\ \eta' \end{pmatrix} = \omega \begin{pmatrix} C & 0 \\ 0 & 1 \end{pmatrix} \begin{pmatrix} v' \\ \eta' \end{pmatrix}, \quad (1)$$

where $A_{11} = \alpha(U_0 C + D^2 U_0) - i C^2 / Re$, $A_{22} = \alpha U_0 - i C / Re$, $C = k^2 - D^2$, $D = d/dy$, and $k^2 = \alpha^2 + \beta^2$. The Reynolds number reads as $Re = U_\infty \delta_* / \nu$, where U_∞ , δ_* and ν are the freestream velocity, displacement thickness and kinematic viscosity, respectively. The ω 's for this semi-bounded domain are either continuous or discrete. We compute samples of the continuous spectrum via a different set of boundary conditions for accuracy as will be discussed in latter sections. For the continuous part of the spectrum, the complex frequencies are given by

$$\omega = \alpha - i(k^2 + \tilde{k}^2) / Re, \quad (2)$$

where $\tilde{k} \in \mathbb{R}^+$ represents the wavenumber in normal direction of the continuous eigenfunctions in the freestream. Equation (2) is obtained by relaxing the condition that it is sufficient for \mathbf{q}' to remain finite for $y \rightarrow \infty$ [24]. Upon substituting ω from Eq. (2) into Eq. (1), we get the eigensystem for the continuous spectrum with \tilde{k}^2 as the eigenvalue.

A. Boundary conditions at the compliant wall

The dynamics of the compliant wall, $y_d = \hat{\xi}_d(x_d, z_d)$ is given by

$$m_d \frac{\partial^2 \hat{\xi}_d}{\partial t_d^2} + d_d \frac{\partial \hat{\xi}_d}{\partial t_d} + [B_d \nabla_d^4 - T_d \nabla_d^2 + K_d] \hat{\xi}_d = -\hat{p}_d(y_d = 0) + 2\mu \left(\frac{\partial \hat{v}_d}{\partial y_d} \right)_{y_d=0}, \quad (3)$$

where $\nabla_d^2 = \partial_{x_d x_d} + \partial_{z_d z_d}$, and m_d , d_d , B_d , T_d and K_d are the wall properties, namely, surface density, damping coefficient, flexural rigidity, wall tension and stiffness constants, respectively. The subscript “ d ” is used to indicate that quantities have their dimensions. The usual nondimensional equation used (e.g., see [20]) is

$$m \hat{\xi}_{tt} + Re^{-1} d \hat{\xi}_t + Re^{-2} [B \nabla^4 - T \nabla^2 + K] \hat{\xi} = \hat{\sigma}_{yy}, \quad (4)$$

where $\hat{\sigma}_{yy} = -\hat{p}_{y=0} + 2Re^{-1} D \hat{v}|_{y=0}$. These equations arise from the following scalings: $m = m_d / (\rho_d \delta_*)$, $d = d_d \delta_* / (\nu \rho_d)$, $B = B_d / (\rho_d \delta_* \nu^2)$, $T = T_d \delta_* / (\rho_d \nu^2)$, and $K = K_d \delta_*^3 / (\rho_d \nu^2)$. Note that the nondimensional values of all wall properties change with δ_* . In a parametric study, where variations in Re are only due to variations in δ_* , such nondimensionalization will make m , d , B , T and K vary with respect to Re . Therefore, following Yeo et al. [19], we opt for a nondimensionalization of the wall properties as $m = m_d / (\rho_d L_d)$, $d = d_d / (\rho_d U_\infty)$, $B = B_d / (\rho_d U_\infty^2 L_d^3)$, $T = T_d / (\rho_d U_\infty^2 L_d)$, $K = K_d L_d / (\rho_d U_\infty^2)$, where $L_d = N_{Re} \nu / U_\infty$. Here, N_{Re} is a number of our choice used to fix the length-scale L_d to a constant. Without any loss of generality, we fix the length-scale L_d by choosing $N_{Re} = 500$. Such a choice of the length-scale as a constant helps in reformulating the boundary condition for Eq. (4), thereby highlighting its explicit dependence on the Reynolds number [19]. Upon using these reference scales, and after substituting the normal modes $(\hat{\xi}, \hat{\sigma}_{yy})^T = (\xi', \sigma'_{yy})^T \exp[i(\alpha x + \beta z - \omega t)]$, Eq. (3) reads as

$$-m \gamma^{-1} \omega^2 \xi' - i d \omega \xi' + C(k, \gamma) \xi' = \sigma'_{yy}, \quad (5)$$

where $C(k, \gamma) = Bk^4/\gamma^3 + Tk^2/\gamma + K\gamma$ and $\gamma = Re/N_{Re}$. It is worth noting that the scaling of m by γ signifies the fact that as one moves downstream, the inertia of the wall becomes relatively less important because of the growth of the boundary layer, which forces us to consider a larger volume of fluid, thus a higher inertia of the fluid.

The kinematic conditions in the primed variables read as,

$$u'(0) = -\xi' DU_0(0), \quad (6)$$

$$v'(0) = -i\omega\xi', \quad (7)$$

$$w'(0) = 0. \quad (8)$$

Note that Eq. (6) is obtained from a first-order Taylor expansion of the no-slip condition, $u'(y = \xi') = 0$. Now, we are able to obtain the wall surface pressure from the x - and z -momentum equations evaluated at the wall:

$$-i\omega u'(0) + DU_0 v'(0) = -i\alpha p'(0) + Re^{-1}(D^2 - k^2)u'|_{y=0} \quad (9)$$

$$-i\omega w'(0) = -i\beta p'(0) + Re^{-1}(D^2 - k^2)w'|_{y=0}. \quad (10)$$

The LHS of Eqs. (9) and (10) are zero due to the kinematic conditions given by Eqs. (6)–(8). Upon adding Eq. (9) and Eq. (10), the wall-pressure is given by

$$p'(0) = (Rek^2)^{-1}(D^2 - k^2) [Dv' + r\eta']_{y=0}, \quad (11)$$

where $r = (\alpha - \beta)/(\alpha + \beta)$. Equation (11) suggests that the perturbed wall-pressure vanishes in the inviscid limit. This is due to the creeping nature of the flow for which there is a complete balancing of pressure gradients in the streamwise and spanwise directions by viscous forces. Hence, in such a limit, the fluid-solid interaction occurs via a one-way coupling, i.e., in the linear first-order case the dynamics of the wall affects the flow without itself being affected by the flow field. Note that this has an important implication on the transient growth as will be explained later.

The amplitudes $u'(y)$ and $w'(y)$ are obtained by continuity and by the definition of η' as $u' = ik^{-2}(\alpha Dv' - \beta\eta')$ and $w' = ik^{-2}(\beta Dv' + \alpha\eta')$. At the wall, using Eq. (11) for p' , one can easily recast $\sigma'_{yy} = -p'(0) + 2Dv'(0)/Re$ as

$$\sigma'_{yy} = Re^{-1} [(3D - k^{-2}D^3)v' - rk^{-2}(D^2 - k^2)\eta']_{y=0}. \quad (12)$$

Now, upon substituting these expressions of σ'_{yy} , u' , w' and ξ' into Eqs. (5), (6) and (8), we derive the boundary conditions for v' and η' at the wall as

$$-\frac{i\omega mk^2}{\gamma}v' = \left[-dk^2 + \frac{i\alpha C(k, \gamma)}{DU_0}D + \frac{3k^2}{Re}D - \frac{D^3}{Re} \right] v' - \left[\frac{i\beta C(k, \gamma)}{DU_0} + \frac{r}{Re}(D^2 - k^2) \right] \eta', \quad (13)$$

$$\omega[-\alpha Dv' + \beta\eta'] = k^2 DU_0 v', \quad (14)$$

$$\beta Dv' + \alpha\eta' = 0. \quad (15)$$

Note that in Eq. (13), the eigenvalue ω appears linearly, although it appeared as a quadratic term in the original Eq (5). This is a direct consequence of the following three substitutions in the LHS of Eq. (5): $\{\omega^2\xi', \omega\xi, \xi'\} \leftarrow \{i\omega v'(0), iv'(0), -u'(0)/DU_0(0)\}$. It is worth highlighting that this step is crucial since it allows us to avoid a nonlinear eigensystem, and thereby circumventing the need to resort to the companion matrix method. This becomes possible as the linear system is inherently not quadratic in the state variable of velocity field. This formulation is clearly economical when it comes to obtaining the eigenvalues. For instance, it drastically reduces the computational effort by a factor of 8 when compared to the formulation of [20], in which all four unknowns $\{u', v', w', p'\}^T$ are collocated across the entire flow domain—the number of unknowns in the present case is only two [25]. For the case of the continuous spectrum, the wall-boundary conditions are obtained by substituting ω from Eq. (2) into Eqs. (13) and (14).

B. Freestream condition for the discrete and continuous spectra

In theory, the freestream boundary conditions are to be satisfied infinitely away from the compliant wall. However, in practice a finite-size domain is considered along with the approximate freestream boundary conditions, which is dependent on the domain size. When a very large domain is considered in the normal direction, the flow at the upper boundary is subjected to the vanishing boundary conditions, $v'(y_{\max}) = \eta'(y_{\max}) = 0$, where y_{\max} is defined by $y \in [0, y_{\max}]$. When the wavenumbers α and β are very small, such vanishing boundary conditions satisfactorily apply only for very large domains, e.g., for domains with $y_{\max} > 150$ in units of displacement thickness. This is because,

at such low wavenumbers, the weak viscous effects require a long distance in the normal direction to damp out the energy injected into the flow by the velocity field of the wall. We verified numerically using a multi-point boundary value problem solver [26] that only for such large domains with $y_{\max} \sim 150$, all higher derivatives of v' and η' vanish for an eigenfunction from the discrete part of the spectrum. However, from the numerical standpoint, when such large domains are considered in combination with large numbers of collocation points or multiple Chebyshev domains, the continuous part of the spectrum gets contaminated, and yields a so-called pseudospectra, see Refs. [23, 27]. It is therefore imperative to find a way to enforce a set of freestream boundary conditions as accurately as possible for domain sizes as small as $y_{\max} = 20$. To this aim, we adopt two different sets of freestream boundary conditions for both the discrete and continuous parts of the spectrum.

For the discrete part of the spectrum, the OS equation—i.e. the first component of Eq. (1)—admits the classical solution $v'(y) = \sum_{j=1}^4 A_j e^{\lambda_j y}$, at the freestream where $\{A_j\}_{j=1, \dots, 4}$ are constants. The four λ_j 's are given by $\lambda_{1,3} = \mp k$ and $\lambda_{2,4} = \mp \sqrt{iRe(\alpha - \omega) + k^2}$ as found in [23]. Among these solutions, λ_3 and λ_4 have a positive real-part leading to nonphysical and exponentially growing modes in the limit of $y \rightarrow \infty$. These are trivially eliminated by setting $A_3 = A_4 = 0$. The second mode is a decaying one, and since λ_2 is proportional to \sqrt{Re} , it should pose no problem in satisfying $v'(y_{\max}) = 0$ at relatively large Reynolds number. However, given $\lambda_1 = -k$, it is possible that the first mode might not decay fast enough to accurately satisfy this freestream condition. For instance, this would be an issue when considering $y_{\max} = 20$ and k as small as 0.05—such a small value is not unrealistic at low Re , especially given that $v'(y=0) \neq 0$ as in our case. Though these conditions may be satisfied for large values of y_{\max} , a sufficiently satisfactory guess would lead to a very large value for y_{\max} , which would result in prohibitively high computational cost. To circumvent this critical issue, we propose a change to the freestream boundary conditions so as to account for the specificities of the exponential decay-rate of the first mode associated with $\lambda_1 = -k$.

For the normal vorticity, it is rather difficult to prescribe the freestream condition from its behavior $\eta'(y) = A_5 e^{\lambda_2 y} + \eta'_p(y)$ due to the functional nature of $\eta'_p(y)$:

$$\eta'_p(y) = \frac{i\beta Re}{\lambda_4 - \lambda_2} \left(e^{\lambda_2 y} \int_0^y DU_0(y')v'(y')e^{-\lambda_2 y'} dy' - e^{\lambda_4 y} \int_0^y DU_0(y')v'(y')e^{-\lambda_4 y'} dy' \right). \quad (16)$$

However, one should note that $w'(0) = 0$, even in the presence of a compliant wall. Therefore, this gives the motivation of retaining $w'(y_{\max}) = 0$ as one normally does for the solid-wall case. Hence, the freestream conditions for the discrete part of the spectrum are given by $Dv' + kv' = 0$, $D^2v' + kDv' = 0$, and $\beta Dv' + \alpha\eta' = 0$ at $y = y_{\max}$.

In the case of the continuous spectrum, the freestream behavior is given by

$$v'(y) = \tilde{A}_1 \exp(i\tilde{k}y) + \tilde{A}_2 \exp(-i\tilde{k}y) + \tilde{A}_3 \exp(-ky), \quad (17)$$

$$\eta'(y) = \tilde{A}_4 \exp(i\tilde{k}y) + \tilde{A}_5 \exp(-i\tilde{k}y) + \eta'_p(y). \quad (18)$$

Reference [28] says that the behavior given by Eq. (17) can be written as $(D^2 + \tilde{k}^2)v' = \tilde{A}_3(k^2 + \tilde{k}^2) \exp(-ky)$, which they implemented as a boundary condition, after removing \tilde{A}_3 , and by evaluating the above equation at two different locations in the freestream. Here, we prefer to implement the above condition at a single location in the freestream upon eliminating the constant \tilde{A}_3 from the derivatives. Consequently, the freestream conditions for the continuous spectrum read as $D^2(D+k)v' = -\tilde{k}^2(D+k)v'$, $D^3(D+k)v' = -\tilde{k}^2 D(D+k)v'$, and $\beta Dv' + \alpha\eta' = 0$.

C. Numerical method

We consider a domain such that $y \in [0, y_{\max}]$, with $y_{\max} = 20$ in the units of displacement thickness $\delta_* = \int_0^\infty (1 - U_0(y)) dy$. We use a Chebyshev spectral method of order $N = 300$ with $N + 1$ Gauss-Lobatto collocation points to solve the eigensystems [Eqs. (1) and its continuous spectrum version]. To map the boundary layer into the Chebyshev domain, we use $y = a_1(1 + y_c)/a_2 - y_c$ with $y_c \in [-1, 1]$, $a_1 = y_s y_b / (y_b - 2y_s)$, $a_2 = 1 + 2a_1/y_b$. Note that y_c can be any of the Gauss-Lobatto points, namely $y_{c,j} = \cos([j-1]\pi/N)$, $j = 1, \dots, N+1$. The singularities originating from the boundary conditions involving no ω nor \tilde{k}^2 were simply removed by means of algebraic operations on the set of Chebyshev coefficients. To carry out the integrations appearing in the following sections, we use the classical quadrature rule $\int_0^\infty f(y)dy = \sum_{j=0}^N W_j f(y_j) (dy/dy_c)_j$. The weights W_j 's are given by $W_j = (b_j/N) \{2 + \sum_{n=2}^N c_n [1 + (-1)^n] (1 - n^2)^{-1} \cos(nj\pi/N)\}$, with the coefficients $\{b_j\}_{j=0, \dots, N}$ given by $b_0 = b_N = 1/2$, and $b_j = 1$ for $(1 \leq j \leq N-1)$, and $\{c_n\}_{n=0, \dots, N}$ given by $c_0 = c_N = 1$ and $c_n = 2$ for $(1 \leq n \leq N-1)$ [23].

III. MODAL ANALYSIS

In the eigensystems for the discrete and continuous spectra, there is a total of 8 parameters, namely $\{\alpha, \beta, Re, m, d, B, T, K\}$ characterizing the flow and compliant wall. Arguably, an exhaustive study in such a large parameter-space would be impractical, if not prohibitive. Therefore, we limit our study by narrowing down to a specific region of interest in the parameter-space. Specifically, we fix the wall parameters such that the flow exhibits different patterns of unstable regions in the sub-parameter-space of (α, β, Re) . The wall has its own phase-speed, c_w which can be calculated as:

$$c_w = \Im \left(\sqrt{(\gamma d)^2 - 4m\gamma C(k, \gamma)} \right) / (2m\alpha), \quad (19)$$

which is, in fact, the imaginary part of the growth rate of the wall perturbation (shown at a later stage of this paper in Eq. (35) divided by the wavenumber). However, this phase-speed is modulated by the damping force, which can be tuned by a frequency dependent forcing term. Therefore, we consider the *free wave-speed* of the wall for fixing the wall parameters. The free wave-speed of the wall, c_w^{free} is given by $c_w^{\text{free}} = \sqrt{\gamma C(k, \gamma)} / m / \alpha$, which is obtained by setting $d \rightarrow 0$ in Eq. (19). If the absolute value of c_w^{free} is small—or within the range of an order of magnitude of the flow speed—the wall can be termed as *soft*. Such soft walls can exhibit instabilities due to different types of modes with more than one region of instability in the parameters space as a consequence of the wall-flow interaction when the frequencies of the wall and flow are in the same range. Hence, we fix the wall parameters to that of a soft wall.

A. Modal stability analysis

Figure 2 shows the spectrum of the streamwise phase-speeds, $c \equiv \omega / \alpha (\equiv c_r + ic_i)$. In this figure, we show three types of characteristic modes, namely: (i) Tollmien-Schlichting (TS) modes, (ii) Traveling Wave Flutter (TWF) modes, and (iii) Static-Divergence (SD) modes that generally coexist in a flow over such compliant soft walls. Among these modes, TWF and DS find their origin in the elastic and damping nature of the wall, respectively.

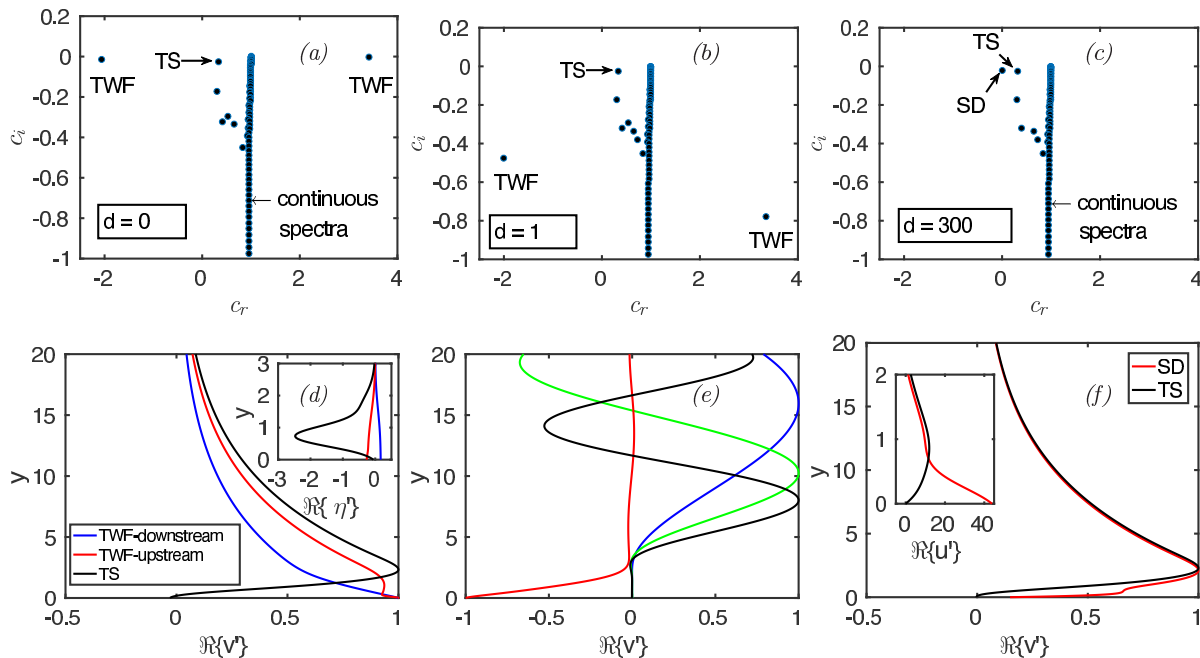


FIG. 2. Spectra and eigenfunctions for $Re = 1000$, $\alpha = 0.1$, $\beta = 0.1$, $m = 2$, $K = 0.3$, $B = 3.2$, $T = 0.75$: (a) $d = 0$; (b) $d = 1$; (c) $d = 300$; (d) Normal velocity v' and vorticity η' of the marked discrete modes in panel (a); (e) Normal velocity of the least-decaying continuous modes in panel (a); (f) Streamwise and normal components, u' and v' respectively, of the marked discrete modes in panel (c).

Across the Figs. 2(a)–(c), the damping-coefficient increases. Figure 2(a) shows two TWF modes—one propagating upstream and the other one downstream—and the TS mode that is the least decaying among all. The adopted method

yields the continuous spectra with extremely reduced distortion compared to previous studies (e.g., see Fig. 3.4(a) in [23]). As the damping coefficient d is increased from 0 to 1, one can note that the TWFs decay faster (see Fig. 2(b)), and completely vanish as d is increased further (see Fig. 2(c)). At very large d values, there appears a new mode, the so-called *Static-Divergence* (SD) mode. We identify this mode as SD following the experimental observation that such mode will have a phase-speed close to zero, and that appears in the case of highly damped walls [12]. Indeed, when d is large, the inertia is primarily balanced by the damping term. Therefore, Eq. (13) gives rise to $\omega \approx 0$. This explains the origin of SD with a phase-speed that is almost zero.

We note that when β is gradually increased from zero, the phase-speed of TWF modes increase as well (not shown here). This is tied to several facts: (1) the TWF modes find their source at the wall, whose phase-speed c_w is given by Eq. (19), (2) these modes originate from the homogeneous part of Eq. (5), and (3) there is a monotonously increasing dependence of c_w on β .

The eigenfunctions of a few selected sample modes are shown in Fig. 2(d-f). Figure 2(d) shows the velocity and vorticity components of the eigenfunctions of two TWF modes and the TS mode of the spectrum shown in Fig. 2(a). The two TWF modes have normal vorticities which are counter-rotating within the boundary layer. The downstream propagating TWF (denoted as “TWF-d”) has a fast and monotonously decaying eigenfunction with respect to the wall-normal coordinate y . Though such monotonicity is absent in the case of the upstream propagating TWF mode (denoted as “TWF-u”), it exhibits maximum at the wall. This indicates that the TWF modes are primarily inviscid in nature, and thereby approximately a solutions to the Rayleigh equation

$$(D^2 - \alpha^2)v'(y) = D^2U_0[U_0(y) - c]^{-1}v'(y). \quad (20)$$

The solution that decays exponentially is given by [29]. The qualitative difference between the profiles of $v'(y)$ for the TWF-u and TWF-d arises from the change in the sign of the term $(U_0(y) - c)$ between these two modes. As the term D^2U_0 is negative in the flow domain, the RHS of Eq. (20) enhances the decay of the TWF-d mode within the boundary layer. Intuitively, this effect can be seen as amplifying the effect of the $-\alpha^2v'(y)$ on the LHS of Eq. (20). In the case of the TWF-u mode, since α^2 is small, Eq. (20) is equivalent to $[D^2 + f(y)]v'(y) = 0$ within the boundary layer, where $f(y) > 0$, which precludes a decaying solution. This phenomenon can be observed in the component $v'(y)$ of these modes as is shown in Fig. 2(d). This behavior of the solutions for both the TWF-d and TWF-u modes can also be observed in a channel flow, where one of the wall is a compliant (e.g., see Figs. 3(a) and 3(b) of [30]), and can be explained through a similar and analogous argument.

Figure 2(e) shows a few eigenfunctions of the continuous spectrum from Fig. 2(a). In the case of flat rigid wall, the freestream fluctuations of the continuous spectrum are kept away due to a rapid quenching near the edge of the boundary layer, a phenomenon known as *shear sheltering* [28]. However, in the present case, these fluctuations are allowed to penetrate the boundary layer, but without the required sinusoidal oscillations in the normal direction so as to match the nontrivial wall-boundary conditions.

Figure 2(f) shows $v'(y)$ and $u'(y)$ for the TS and SD modes shown in Fig. 2(c). Though their normal velocity component $v'(y)$ hardly differ, the streamwise components $u'(y)$ of TS and SD modes differ notably. The SD mode exhibits a stronger streamwise component $u'(y)$ near the wall.

The unstable regions are now presented in the parameter-spaces of $Re - \alpha$ and $\alpha - \beta$, for a chosen set of other parameters. Figure 3 shows the same contours but now for the flow over a compliant wall with varying wall properties. In these figures, the neutral curve (i.e., contour level 0.00) serves as the separating boundary between the unstable and stable regions.

Across Figs. 3(a)–3(d), the damping coefficient d increases while the other wall parameters have been set to that of a soft wall except for Fig. 3(f). One may note that the flow can develop instabilities for practically all values of the Reynolds number, except for Fig. 3(f) where the flow exhibits stability at low Re . This is because Figs. 3(a)–(e) correspond to a soft wall, while Fig. 3(f) is obtained for a nonsoft wall. The instability regions at low Re in Figs. 3(a)–(e) arises from the hydroelastic nature—e.g., due to the presence of unstable static divergence modes when the damping parameter d is large, or due to an unstable near-stationary *transitional mode*, which appears due to the merging of TS and TWF modes [13, 31] when d is small. In the higher Re regime, the unstable modes are of the usual TS kind and exists in the solid-wall case where these modes travel with a finite phase-speed lower than the freestream velocity. This identification can be justified based on the phase speeds of these modes which, will be presented subsequently.

For low values of d , the unstable zone extends to a region including greater values of α . For the lowest value of d considered ($d = 1$ in Fig. 3(a)), the regions of instability due to the near-stationary transitional modes and the traveling TS modes merge to form a larger unstable region in this parameter space. However, the dominant unstable mode in this region is of the traveling TS kind. However, for larger values of d , the instability regions of these two types of unstable modes become distinct, where the near-stationary transitional unstable mode is dominant at low Re , while the traveling TS mode dominates in the higher Re regime as shown by Fig. 3(d). Figure 3(e) is for a very low value of K in comparison with Figs. 3(a)–(d). At such low value of K , the phenomenon of larger region of the

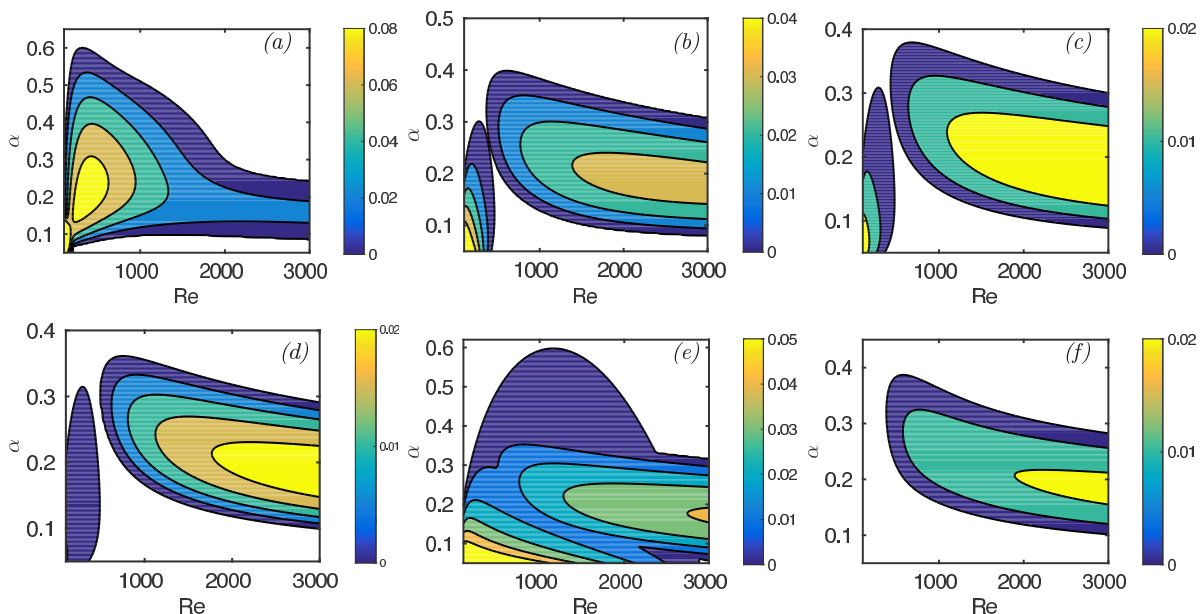


FIG. 3. Contours of $c_i = \Im(c)$, with $c \equiv \omega/\alpha$, in the $Re - \alpha$ plane with $\beta = 0$, $T = 0.1$, $B = 0.2$ and $m = 2$: (a) $d = 1$, $K = 0.05$; (b), (c) and (d) are for $d = 10, 20, 100$ respectively with other parameters identical to (a); (e) $d = 10$, $K = 0.005$, $B = 0.2$, $T = 0.1$; (f) $d = 10$, $K = 0.5$, $B = 0.2$, $T = 0.1$.

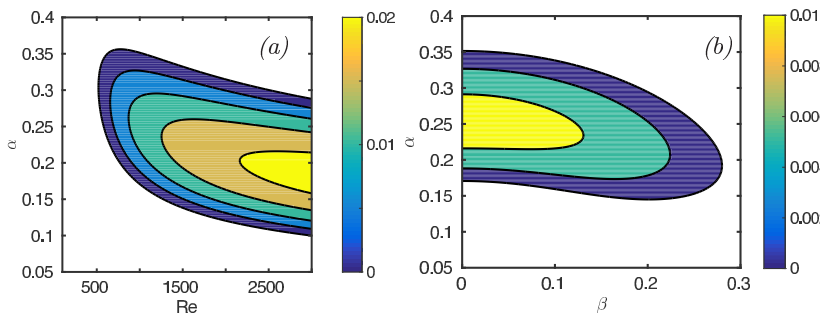


FIG. 4. Contours of $c_i = \Im(c)$ for a rigid wall: (a) in (Re, α) plane with $\beta = 0$; (b) in (α, β) plane with $Re = 1000$.

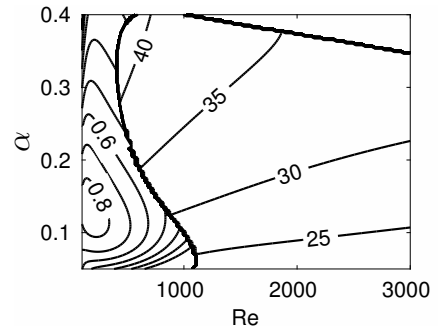


FIG. 5. Contours of $c_r \times 100$ for the case of Fig. 3(c).

parameter space becoming unstable is common with the situation for the case of low values for d as shown in Fig. 3(a). However, there is a subtle difference in the pattern of the values of the growth rate between Figs. 3(a) and (e). This difference stems from the fact that decreasing d increases the natural phase-speed of the wall (See, Eq. 19), while decreasing K does the opposite. These opposite natures of the wall-phase-speed are also reflected in the fluid-wall coupled phase-speed (c_r) of the modes corresponding to Fig. 3(a) and (e) (not shown here). In fact, the pattern in Fig. 3(e) is similar to the case of Fig. 3(b), where these two differ only in the values of K . Upon reducing K , the instability due to near-stationary transitional modes merges with the region of instability caused by the traveling TS mode, but differs from the case of Fig. 3(a) by not affecting the nature of traveling TS mode being dominant in its corresponding location in the plane of $Re - \alpha$.

Figure 3(f) is for a high value of K . The instability associated with the near-stationary transitional modes vanishes altogether due to such high stiffness—the wall behaves more like a flat-rigid one. Nonetheless, the critical Reynolds number of the viscous instability is much lower in comparison with the rigid-wall case—the c_i levels are significantly higher than those for the rigid-wall case at a chosen Re . Furthermore, we observe that increasing K , B and T results in recovering the results for the rigid-wall case since these parameters all tend to increase the wall-phase-speed. However, it should be noted that among these wall parameters, only K has more pronounced effect, followed by T and then by B .

Upon comparison of Fig. 3(f) with the corresponding contours for a non-compliant rigid wall shown in Fig. 4(a), it should be noted that the flow over the compliant wall, in the rigid-wall limit, exhibits higher instability than the

corresponding flow in the non-compliant rigid wall case. The instabilities in both figures are due to TS modes. The difference in growth rates can be explained through the classification due to [32] and [8]. Under this classification, TS and TWF modes belong to Class A and Class B, respectively, while the near-stationary transitional and SD modes fall into the Class C category. Therefore, any phenomenon that stabilizes Class-A modes will destabilize Class-B ones, and *vice versa* [31]. Since the wall damping in Fig. 3(f) stabilizes the TWF mode (see Fig. 2), it exhibits enhanced TS mode instability when compared to the non-compliant rigid-wall case.

Figure 5 shows the streamwise phase-speeds ($\Re\{c\}$) corresponding to Figs. 3(c). One may observe that the unstable modes at low Re are almost stationary, which is further verified for other set of parameters in Fig. 3. However, their phase-speed increases with decreasing d as can be seen in Fig 6(a), which shows the unstable mode for a range of the parameter d varying from 0 to 20. As d is increased, the traveling TS mode gets converted into a near-stationary transitional mode. Figure 6(b) shows the evolution of the phase-speed and growth-rate of a TS mode with the stiffness constant K . In this figure, the least-decaying (or equivalently the fastest-growing) mode shown is not stationary—i.e., the phase-speed is not close to zero—due to the low value of the damping coefficient d . Except for K , the rest of the parameters has been set to that of Fig. 3(a). As K increases, the phase-speed saturates to a constant value, and the mode gets stabilized gradually, thereby suggesting the destabilizing nature of a soft compliant wall.

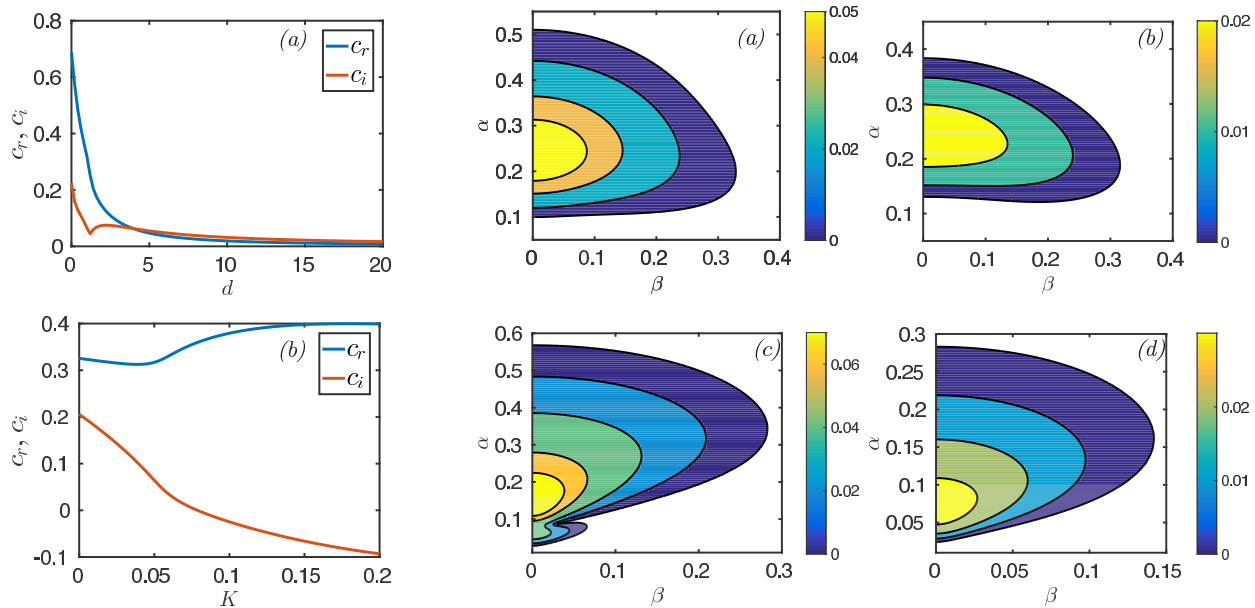


FIG. 6. c_r and c_i for $Re = 200$, $\alpha = 0.1$, $\beta = 0$, $m = 2$, $B = 0.2$, $T = 0.1$: (a) versus d with $K = 0.05$; (b) versus K with $d = 1$.

FIG. 7. Iso-contours of c_i in $\alpha - \beta$ plane with $K = 0.05$, $B = 0.2$, $T = 0.1$: (a) $Re = 1000$ and $d = 1$; (b) $Re = 1000$ and $d = 10$; (c) $Re = 200$ and $d = 1$; (d) $Re = 200$ and $d = 10$.

Figure 7 shows the unstable region in the $\alpha - \beta$ plane with other parameters set to that of a soft wall to ensure that we are in the presence of near-stationary transitional unstable modes whenever Re is low. Figures 7(a) & 7(b) show that the instability due to the traveling TS modes spreads to higher values of β in comparison to the flat-rigid-wall case (shown in Fig. 4(b)) suggesting that the oblique modes are prone to more instability due to wall compliance. As observed in Fig. 3, the unstable α -band diminishes upon increasing d as evident from the comparison of Fig. 7(a) with Fig. 7(b). The fact that these unstable modes are of the traveling TS kind can also be verified from the contours of phase-speeds (not shown here), which were all found to be above the level 0.3. The unstable region associated with the near-stationary modes at low Re has been shown in the $\alpha - \beta$ plane in Figs 7(c) & 7(d) at low values of α and β . Although they appear only in the compliant-wall case, they exhibit a clear signature of interaction with the flow through the shapes of these contours. Indeed, if these instabilities are to be attributed prominently to the wall, one would expect a circular symmetry of these contours since the governing Eq. (5) possesses such symmetry in the $\alpha - \beta$ plane. One should note that for these modes at low Re , α and β can be understood from the variations of the phase-speed of the wall shown in Eq. (19). Specifically, when both α and β are small—i.e., when k is small, the contribution due to flexural rigidity and tension are negligible. In such situations, Eq. (19) indicates that c_w decreases with decreasing Re or decreasing K . In other words, for low values of α and β , the effect of a decrease in Re on the instability due to hydroelastic modes is similar to the effect of a decrease in K . As can be seen from Fig. 6(b), a decrease in K causes instability, so is when Re is decreased. This leads to the observed unstable regime at low Re .

The comparison of Fig. 7(c) and Fig. 7(d) implies that such destabilizing interaction between the flow and the wall

decreases with an increase of d as one would expect, it reduces the effective forcing by the fluid.

B. Modal energy analysis

We analyze the least-decaying mode in order to identify the root causes of the instability mechanisms in terms of its constituent energies channeled through different routes: e.g., via the meanflow, viscous dissipation, wall damping, or the work done on the surface by the fluid. The total perturbation energy is defined as

$$E'(t) = \frac{e^{2\omega_i t}}{2k^2} \left(\int_0^\infty (k^2 |v'|^2 + |Dv'|^2 + |\eta'|^2) dy + k^2 (m\gamma^{-1} |\omega \xi'|^2 + C(k, \gamma) |\xi'|^2) \right). \quad (21)$$

Given our formalism based on the set of working variables (v', η') , one can rewrite this energy as

$$E'(t) = \frac{e^{2\omega_i t}}{2k^2} \int_0^\infty \begin{pmatrix} v' \\ \eta' \end{pmatrix}^T \begin{pmatrix} k^2 + D^T D + \delta(y) \left[k^2 \left(\frac{m}{\gamma} + \frac{C(k, \gamma)}{|\omega|^2} \right) \right] & 0 \\ 0 & 1 \end{pmatrix} \begin{pmatrix} v' \\ \eta' \end{pmatrix} dy, \quad (22)$$

where $\delta(y)$ is the Dirac δ -distribution. Using the identity $\int_0^\infty |Dv'|^2 dy = (v'^* Dv')_{y=0} - \int_0^\infty v'^* D^2 v' dy$, and Eq. (1), the rate-of-change of the perturbation energy reads as

$$\frac{dE'}{dt} = \frac{dE'_w}{dt} - \frac{e^{2\omega_i t}}{2k^2} \left(i \int_0^\infty \mathbf{q}'^T A \mathbf{q}' dy + i\omega v'^*(0) Dv'(0) + \text{c.c.} \right), \quad (23)$$

where $\mathbf{q}' = (v', \eta')^T$, A is the coefficient-matrix on the LHS of Eq. (1), “c.c.” denotes the complex conjugate terms, the superscript $*$ corresponds to the complex conjugation operator, and $E'_w = v'(0)^* (m\gamma^{-1} + C(k, \gamma) |\omega|^{-2}) v'(0) \exp[2\omega_i t]/2$. Using the boundary conditions (14) and (15), one can easily show that $i\omega v'^*(0) Dv'(0) + \text{c.c.} = 0$, and thus using Eq. (5), one arrives at

$$\frac{dE'_w}{dt} = \frac{e^{2\omega_i t}}{2Re} \left(-dRe |v'(0)|^2 + 3v'^*(0) Dv'(0) - \frac{v'^*(0) D^3 v'(0)}{k^2} + \text{c.c.} \right). \quad (24)$$

In summary, Eq. (23) can be written as the sum of four distinct terms: $dE'/dt = e^{2\omega_i t} \sum_{j=1}^4 \dot{E}'_j$, where the $\{\dot{E}'_j\}_{j=1, \dots, 4}$ are the rates of energy transfer via different routes, namely by mean-shear (\dot{E}'_1), viscous dissipation (\dot{E}'_2), wall-damping (\dot{E}'_3), and by the forcing associated with the normal stress on the wall (\dot{E}'_4). The explicit expressions for these four terms are

$$\dot{E}'_1 = -i(2k^2)^{-1} \int_0^\infty DU_0 (\alpha v'^* Dv' + \beta \eta'^* v') dy + \text{c.c.}, \quad (25)$$

$$\dot{E}'_2 = -(2k^2 Re)^{-1} \int_0^\infty [\eta'^* (k^2 - D^2) \eta' + v'^* (k^2 - D^2)^2 v'] dy + \text{c.c.}, \quad (26)$$

$$\dot{E}'_3 = -d |v'(0)|^2, \quad \dot{E}'_4 = (2k^2 Re)^{-1} \{ 3k^2 v'^*(0) Dv'(0) - v'^*(0) D^3 v'(0) \} + \text{c.c.} \quad (27)$$

In Eqs. (25)–(27), the eigenfunctions are employed after normalizing them such that they have a unit initial energy, $E'(0) = 1$.

Figure 8 shows the variations of each of these rates of energy transfer \dot{E}'_j with respect to α and β . To analyze the two different modes of instabilities (i.e., due to transitional modes and TS modes), where one is present at very low Reynolds numbers and the other in the regime of low to large Re , we carry out an energy budget analysis for two values of Re , specifically $Re = 200$ and $Re = 1000$. When the analysis is made with respect to α , we fix $\beta = 0$, and when it is made with respect to β , we fix $\alpha = 0.25$. Also shown in Fig. 8 is the total energy-transfer-rate, $\dot{E}' \equiv 2\Im(\omega)$.

Figure 8(a) shows the analysis of the transitional mode with respect to α for $Re = 200$. This corresponds to the analysis along the line $Re = 200$ in Fig. 3(b). It reveals that in the region of α considered, viscous effects have a clear destabilizing effect on the flow, as attested by the positive values of the energy transfer rate \dot{E}'_2 . However, it is worth noting that this rate becomes negative in the same range of α but at higher Re as shown in Fig. 8(b) where an analysis of a TS mode is carried out. This brings to light the dual nature of viscous effects for this particular flow at various Reynolds numbers. At low Re (see Fig. 8(a)), the rate of energy transfer from the meanflow (\dot{E}'_1) is such that it contributes to the instability at very low values of α , and *vice versa* at high values of α . Therefore, at low Re , two-dimensional perturbations are prone to long wave instability caused by the mean-shear. However, as evident from

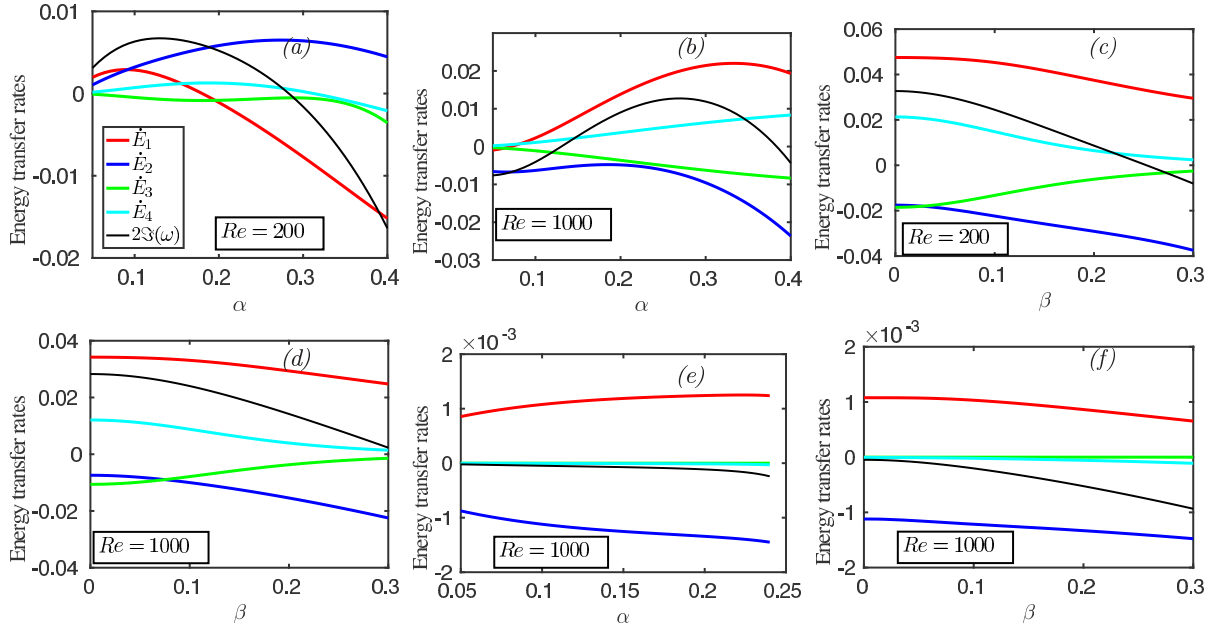


FIG. 8. Energy transfer rates in terms of constituent channels: Red — transfer-rate by mean shear; Blue — transfer rate by viscous dissipation; Green — the transfer rate by wall-damping; Cyan — the transfer rate via forcing by normal stress on the membrane; Black — the total transfer rate: (a) “transitional” mode with $Re = 200$, $\beta = 0$, $m = 2$, $d = 10$, $B = 0.2$, $T = 0.1$, $K = 0.05$; (b) TS mode with parameters same as (a), but for $Re = 1000$; (c) transitional mode with $Re = 200$, $\alpha = 0.25$, $m = 2$, $d = 1$, $B = 0.2$, $T = 0.1$, $K = 0.05$; (d) Same as (c) but for $Re = 1000$; (e) TWF mode with $Re = 1000$, $\beta = 0$, $m = 2$, $d = 0$, $B = 0.2$, $T = 0.1$, $K = 0.05$; (f) TWF with $Re = 1000$, $\alpha = 0.1$, $m = 2$, $d = 0$, $B = 0.2$, $T = 0.1$, $K = 0.05$.

Fig. 8(b), the mean-shear predominantly causes an instability for a wider band of wavenumbers at high Re where the least-decaying mode is of TS kind.

The transfer rates due to the compliant wall, \dot{E}'_3 (wall-damping) and \dot{E}'_4 (fluid-forcing), cancel each other at low Re and low α as shown in Fig. 8(a). However, in the regime of low Re and high α , the compliant wall has a clear stabilizing effect as attested by the negative values of both \dot{E}'_3 and \dot{E}'_4 . In the high- Re regime (see Fig. 8(b)), both of these terms are almost canceling each other for all values of α .

The energy transfer rate due to viscosity, \dot{E}'_2 at low Re turns negative upon reducing the wall-damping parameter d , as evident from the comparison of Fig. 8(a) ($d = 10$) and Fig. 8(c) ($d = 1$). From these subfigures, one can notice that the signs are opposite at the common point of $(\alpha, \beta) = (0.25, 0)$.

Upon increasing the obliquity (i.e., the spanwise wavenumber β) of the perturbations, the qualitative nature of the variations of these individual terms remains constant for low, as well as high Re , as displayed in Figs. 8(c) & 8(d).

Figures 8(e) & (f) show these four energy transfer rates for a TWF mode propagating downstream. As the TWFs have significant growth/decay rate at low d , we have set $d = 0$, and have shown these rates as a function of α in Fig. 8(e) and β in Fig. 8(f). One can note that this TWF-d mode is always stable given the negative net-rate ($2\Im\{\omega\}$) for all α and β . This is in good agreement with its classification as a Class-B mode [14, 31], which allows it to be either negative-energy or positive-energy waves. In the present case this TWF-d is a negative-energy wave which causes irretrievable loss of energy at all wave numbers. Even the component due to the forcing by the fluid on the wall (\dot{E}'_4) is negative, which implies that in effect the fluid interaction actually dampens the wall motion.

For all these different kinds of modes, we found that the sign of the sum of \dot{E}'_3 and \dot{E}'_4 alone predicts qualitatively whether the flow is stable or otherwise at a chosen α or β (not shown here, but a careful look on the green and cyan curves of the panels of Fig. 8 makes this point clear). This phenomenon can be explained through an analogy with the dynamics of a forced-damped pendulum. Such an analogy is suggested by the fact that the governing equation of the wall [see Eq. (5)] is a simple harmonic equation with both forcing and damping terms.

Since the forcing term σ'_{yy} is complex, its phase can be tuned by the variations in Re , α and β . This forcing term plays a crucial role in causing stability/instability, as it can either enhance or hamper the growth of the wall displacement depending on the value of its phase. Equation (5) can be written as $[-m\gamma^{-1}\omega^2 + C(k, \gamma)]\xi' = f'$, where $f' = \sigma'_{yy} + i\omega d\xi'$ plays the effective role of a forcing term. Let us write $f' = |f'|e^{i\phi_1}$ and $v'(0) = |v'(0)|e^{i\phi_2}$, with the phase difference being $\phi = \phi_1 - \phi_2$. When $\phi = 0$, a resonant instability occurs as the effective forcing term is in phase

with the velocity. This instability could occur for any $\phi \in (-\pi/2, \pi/2)$ since the average effective forcing in a cycle yields an increase in $|\xi'|$. The instability vanishes for $\phi \in (\pi/2, 3\pi/2)$.

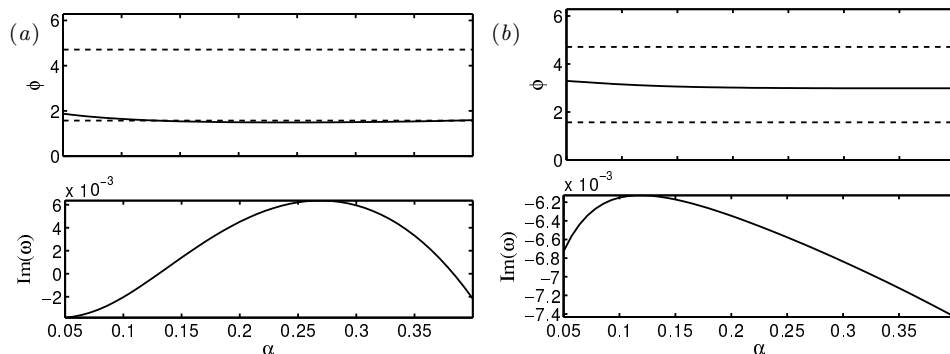


FIG. 9. Phase difference, $\phi = (\phi_1 - \phi_2)$ (top) and growth rate $\Im(\omega)$ (bottom) versus α for $Re = 1000$, $\beta = 0$, $m = 2$, $d = 10$, $B = 0.2$, $T = 0.1$, $K = 0.05$ (same parameters as in Fig. 8(b)): (a) least-decaying mode; (b) second least-decaying mode. The dashed line marks the value of $\pi/2$ and $3\pi/2$.

Figure 9 shows the growth rate $\Im(\omega)$ and the phase-difference ϕ versus α for the flow and wall parameters set as identical to those in Fig. 8(b). Figure 9(a) shows these results for the least-decaying (i.e., the most unstable) mode and Fig. 9(b) is for the second least-decaying mode. As expected, when the phase difference is such that $|\phi| < \pi/2$, the growth rate turns positive for a wide range of values of α as is shown in Fig. 9(a). At both ends of the instability regime, i.e., as the growth rate approaches zero in Fig. 8(a), the phase difference approaches the value of $\pi/2$. When $|\phi| = \pi/2$, the effective forcing term f' produces an increase in ξ' for half of a cycle, and equally hinders it for the other half, thereby causing marginal stability.

The situation is reversed for the second least-decaying mode shown in Fig. 9(b). In the α -range of stability, as anticipated, we obtain $|\phi| < \pi/2$. Here, the stability occurs as the forcing due to the normal stress is opposing the oscillation of the wall for the most part of the cycle. We confirm that this result holds for the other modes as well.

IV. TRANSIENT GROWTH STUDY

Since the linearized Navier–Stokes operator is nonnormal, the eigenfunctions can be nonorthogonal, thus resulting in a transient temporal growth of the norm of a superposition of such eigenfunctions. However, it is worth noting that each term of such a superposition, taken individually, can be asymptotically stable. Such a transient growth is inviscid for flows over solid surfaces, where the viscosity hinders the growth only at a later time. It has been established that in the case of the boundary layer flow over a solid wall under parallel flow approximation, the temporal maximum of the transient growth is proportional to Re^2 for streamwise independent modes (i.e., for $\alpha = 0$) [33]. Such transients are responsible for the transition to turbulence in the subcritical regime by amplifying the infinitesimal perturbation to sufficiently finite amplitude susceptible to the action of nonlinearity.

Let us consider the following superposition of modes

$$\tilde{\mathbf{q}} = \sum_{n=1}^{K_1} \kappa_n \mathbf{q}'_n(y; \alpha, \beta) \exp(i\omega_n t), \quad \text{with } \mathbf{q}'_n = \{v'_n, \eta'_n, v'_n/\omega_n\}^T, \quad (28)$$

where the subscript n runs over a selected set of K_1 eigenfunctions, and $\{\kappa_n\}_{n=1, \dots, K_1}$ are constants. The integer K_1 is chosen such that (28) includes a sufficient number of modes relevant to the transient growth. This latter point is further discussed in what follows. To quantify the size of $\tilde{\mathbf{q}}$, we use the definition (22) for the total energy of the system (fluid+wall), which is recast as $\tilde{E}(t) = (2k^2)^{-1} \int_0^\infty \tilde{\mathbf{q}}^T \mathbf{M} \tilde{\mathbf{q}} dy$, where the matrix \mathbf{M} is

$$\mathbf{M} = \begin{pmatrix} k^2 + D^T D + \delta(y)k^2 m/\gamma & 0 & 0 \\ 0 & 1 & 0 \\ 0 & 0 & \delta(y)k^2 C(k, \gamma) \end{pmatrix}. \quad (29)$$

Following the same methodology as in [23], the growth rate at an instant t is defined as $G(t) \equiv \max_{\kappa_n} (\tilde{E}(t)/\tilde{E}(0)) = \|\mathbf{F} \exp(i\mathbf{\Omega}t) \mathbf{F}^{-1}\|_2$, where $\mathbf{\Omega} = \text{diag}\{\omega_n\}$ where $n = 1, \dots, K_1$, $\mathbf{F}^T \mathbf{F} = \mathbf{A}$ with $A_{ij} = (2k^2)^{-1} \int_0^\infty \mathbf{q}'_j^T \mathbf{M} \mathbf{q}'_i dy$. Furthermore, the maximum growth rate is given by $G_{\max} \equiv \max_{t>0} G(t)$ with t_{\max} defined such that $G(t_{\max}) = G_{\max}$.

We now present results on transient growth and optimal perturbations for small values for α and β to ward off the pseudospectra. Figure 10(a) shows the growth rate $G(t)$ of modes that are approximately independent of the

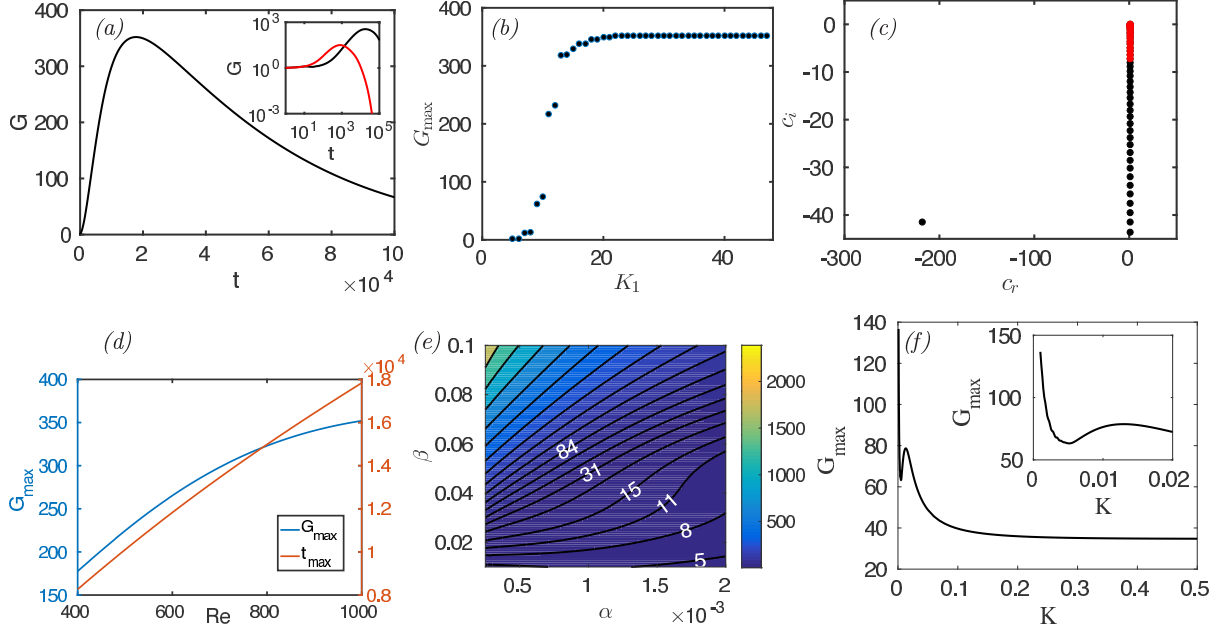


FIG. 10. Transient growth: (a) Black line is $G(t)$ for $Re = 1000$, $m = 2$, $d = 1$, $K = 0.3$, $B = 3.2$, $T = 0.75$ $\alpha = 0.001$ and $\beta = 0.09$; the red line in the inset corresponds to the solid-wall case; (b) G_{\max} versus no. of modes K_1 in the superposition; (c) The red-part of the spectrum contributes to 99% of G_{\max} ; (d) G_{\max} and t_{\max} versus Re ; (e) G_{\max} in $\alpha - \beta$ plane with other parameters as in (a); and, G_{\max} and versus K .

streamwise direction (i.e., with $\alpha \approx 0$). The wall- and flow-parameters have been set in the stable regime. It should be noted that t_{\max} is nearly 2×10^4 , which is in contrast to that of a solid wall where $t_{\max} \approx 778$ [21]. Also shown in the inset of Fig. 10(a) is the comparison with the solid-wall case (red line).

As $t_{\max} \sim \mathcal{O}(10^4)$ (see Fig. 10(a)), which is a fairly large value, the transient growth can be fully described by a set of least-decaying modes. For this reason, we estimate that considering $K_1 = 50$ modes is vastly sufficient for all our calculations given that low values are considered for α and β . Figure 10(b) shows the contribution of each mode (in the order of their decay-rate) to G_{\max} , thus showing the convergence with respect to the number of modes. Figure 10(c) shows the region of the spectrum (marked red) that contributes most to the transient growth.

Figure 10(d) shows the dependence of G_{\max} and t_{\max} on the Reynolds number. Though t_{\max} varies linearly with Re as in the solid-wall case, the maximum growth rate G_{\max} does not preserve the quadratic growth with respect to Re , which is a trend commonly observed for parallel flows over solid walls [33]. With our soft compliant wall, G_{\max} increases at a rate slower than a linear dependence or Re . It is worth noting that the quadratic growth in the solid-wall case is theoretically supported for such streamwise-independent modes [34]. However, in the compliant-wall case, the wall-boundary condition has a significantly more complex dependence on the Reynolds number. This results in an inability to absorb the entire system's Re -dependence by a scaling of the dependent variables—a step required in order to establish the quadratic dependence on Re .

Figure 10(e) shows the contours of G_{\max} in the $\alpha - \beta$ plane. The supremum of G_{\max} appears for a mode with vanishing α . This fact is consistent with what is observed with the boundary layer flow over a solid wall, and one can expect streaks to form the optimal patterns. A contrasting aspect is the rapid increase in G_{\max} with respect to β , which is at much higher rate than that of such flow over a solid wall [35]. Such rapid increase is a signature of the higher nonnormality of the underlying linear operator than that of the flat-rigid wall case. This causes the computation to become more sensitive to the accuracy of the pseudospectra even at such low values of wavenumbers. As a consequence, with the current double-precision accuracy, it is impossible to capture the optimal value for β .

Figure 10(f) displays the variation of G_{\max} with respect to the stiffness constant K for three-dimensional modes. Overall, G_{\max} decreases when the wall undergoes transition from a soft one (i.e., with low K) to a hard one, and this trend saturates for $K > 0.3$. This suggests that, in the case of a soft compliant wall, there exists a mechanism of transient growth apart from the inviscid growth that normally exists in the solid-wall case. We anticipate this to be a combination of pressure and viscous forces on the wall. As the transient growth is predominantly due to the

nonorthogonality of continuous modes within the boundary layer, the difference in the G_{\max} between the solid- and compliant-wall cases should hail from these modes. These continuous modes have a nonvanishing boundary behavior as can be seen in Fig. 2(e). Therefore, the inner product of these functions can naturally be higher compared to the solid-wall case, where these functions have a vanishing boundary behavior. Thus, the wall compliance enhances the nonorthogonality of the eigenfunctions, making them susceptible to a stronger transient growth. The role of viscosity in enhancing the transient growth is further confirmed in Sec. IV B by means of a term-by-term energy budget analysis.

A. Optimal patterns and their origins

We now turn to the problem of finding the coefficients $\{\kappa_n\}_{n=1,\dots,K_1}$ in Eq. (28) that take the superposition $\tilde{\mathbf{q}}$ to the state of maximum energy, i.e., $\tilde{E}(t_{\max}) = G_{\max}$. This set of $\{\kappa_n\}_{n=1,\dots,K_1}$ satisfying $E(t_{\max}) = G_{\max}$ can be found by means of $\boldsymbol{\kappa} = \mathbf{F}^{-1}\mathbf{U}(:, 1)$, where \mathbf{U} is the unitary matrix arising from the following singular value decomposition: $\mathbf{F} \exp(i\boldsymbol{\Omega}t)\mathbf{F}^{-1} = \mathbf{U}\mathbf{S}\mathbf{V}^T$. With the obtained vector $\boldsymbol{\kappa} = (\kappa_1, \dots, \kappa_{K_1})^T$, we have $\tilde{\mathbf{q}}(t=0)$ denoted as the *initial perturbation* and $\tilde{\mathbf{q}}(t=t_{\max})$ as the *optimal perturbation*. Figures 11(a) & 11(b) show the initial and optimal patterns of perturbation velocities in the (x, y) plane, while Fig. 11(d) & 11(e) show the same in the (y, z) plane.

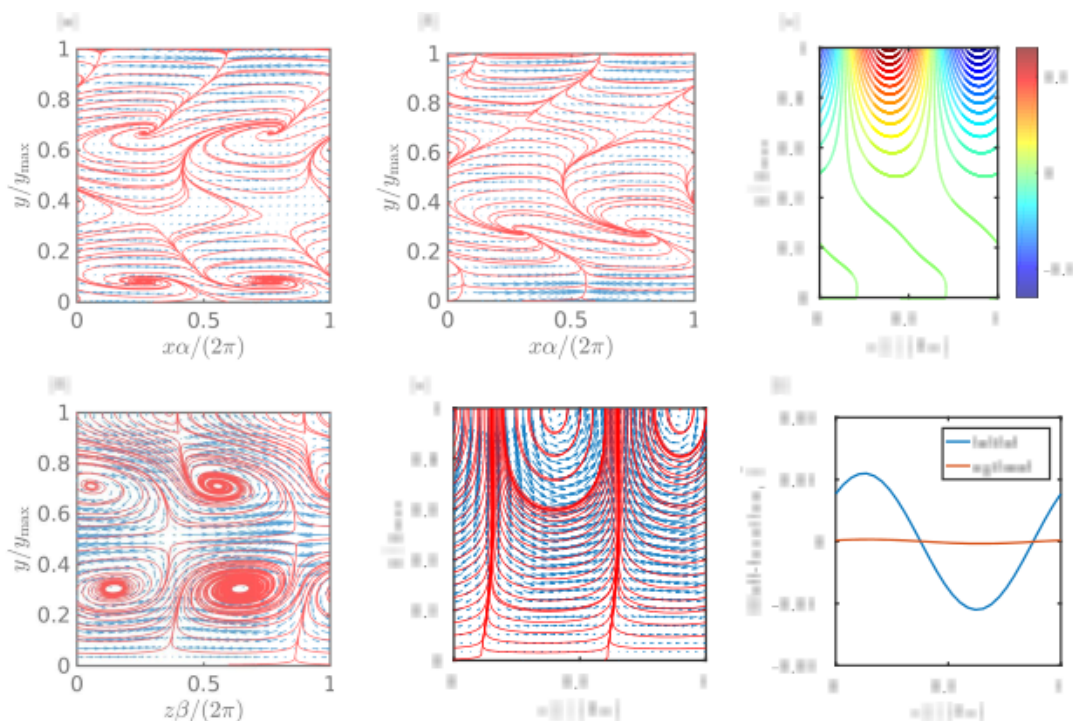


FIG. 11. Initial and optimal perturbations for $Re = 1000$, $m = 2$, $d = 1$, $K = 0.3$, $B = 3.2$, $T = 0.75$: (a) and (b) are initial and optimal patterns of perturbation velocities, respectively, with $\alpha = 0.002$, $\beta = 0$ in (x, y) plane (Red lines show streamlines); (c) is contours of streamwise optimal perturbation velocity in (y, z) plane with $\alpha = 0.00025$, $\beta = 0.09$; (d) and (e) initial and optimal patterns of perturbation velocities, respectively, corresponding to (c); (f) the initial and optimal wall fluctuation.

In the case of 2D modes, the initial and optimal patterns are expected to follow the classical Orr-mechanism. To contrast against the flat-rigid wall case, we show the optimal patterns for such a case in Fig. 12 with $\alpha = 0.1$. We have chosen such large value of α , as the flat-rigid wall boundary layer does not exhibit transient growth at the value of α of Fig. 11(a). In the flat-rigid wall case, the initial pattern associated with the 2D modes is such that the perturbation velocities in the (x, y) plane are in the direction opposing the mean-shear, as shown in Fig. 12(a). The streamlines are tilted against the meanflow within the boundary layer. This perturbation structure gets tilted in the direction of the mean-shear at the later optimal time. However, this particular phenomenon is absent in the present boundary layer flow over a compliant wall as shown in Fig. 11(a) & 11(b). This is because the circulation is not conserved in the present case, even in the inviscid limit. Such a conservation of circulation (i.e., $D\Gamma/Dt = 0$) is a prerequisite for the Orr-mechanism to take place: when such conservation is ensured, the elongated contours tilted against the flow and outlining the constant vorticity/streamlines in the fluid-material undergoes modifications by the natural fluid motion

such that their lengths get shortened until a point of time where the maximum of the transient growth happens, thus causing an increase in the velocity field so as to conserve the circulation. In the compliant-wall case, there is a dynamic entry of vorticity into the flow domain. One can view this wall-dynamics as some sort of forcing on the velocity of a flow over an otherwise flat-rigid wall, and this force, owing to time-dependency and wall dissipation, is not conservative. It can be deduced that the circulation is not conserved in such situation by the same analysis used to arrive Kelvin's theorem. Not surprisingly, this results in notably different initial and optimal patterns.

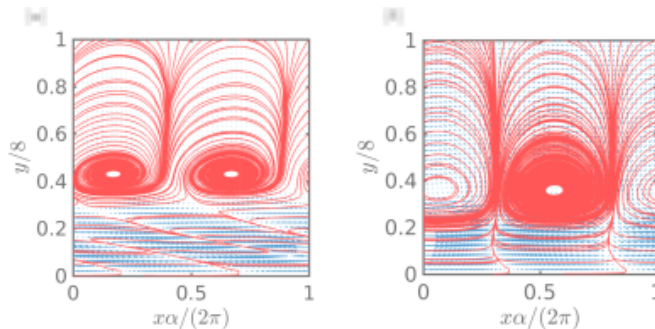


FIG. 12. Initial (a) and optimal (b) perturbations in the case of flat rigid wall with $Re = 1000$, $\alpha = 0.1$, and $\beta = 0$ in (x, y) plane (Red lines show streamlines).

In the case of nearly streamwise-independent modes ($\alpha \approx 0$), the initial and optimal patterns shown in Fig. 11(d) & 11(e) contrast with the observations for the solid-wall case [21] with the cores of the counter-rotating vortices being located at a farther distance away from the wall. The corresponding streaks are shown in Fig. 11(c). Figure 11(f) shows the optimal pattern of the wall in the spanwise direction. The minimum and maximum of the wall pattern at initial time match with the locations of suction and impingement of the flow-fields, respectively, at optimal time as shown in Figs. 11(e) & 11(f). As time evolves towards the optimal instant, these suction and impingement decrease the spatial amplitude of the wall in order to retrieve some potential energy so that the velocity field can have access to it. From Eq. (6), such reduction in wall amplitude implies a reduction in the streamwise component of the velocity field. In turn, this causes the streaks to shift upwards as observed. The structure at optimal time is similar to that of the rigid-wall case—except for the fact that is farther away from the wall—due to the lift-up mechanism: the normal velocity induces the normal vorticity. We believe that the observed phenomena is an interactive effect with the wall. The fluid energy near the wall is minimum as one can see from the lengths of the arrows in Fig. 11(e) and the contour levels in Fig. 11(c). As there is little variations in the magnitude of vectors and contour levels, one can also see that the viscous dissipation is very low for such optimal patterns.

B. Transient energy budget analysis

In the same spirit as the previous modal study, we consider carrying out a transient energy budget study for the superposition of modes $\tilde{\mathbf{q}}$, as this will help us gain insight into the mechanisms of the transient growth. Here, the method described in [36] is followed to calculate nonmodal energy. When compared with the solid-wall case, the transient growth characteristics for the compliant-wall case has primarily two contrasting features: (i) the transient amplification is larger though slower compared to the solid-wall case (see Fig. 10(a)); (ii) for modes with vanishing α , apart from the collapse of the scaling $G_{\max} \sim Re^2$, the growth rate of G_{\max} with respect to Re decreases with increasing Re as can be seen from Fig. 10(d) (i.e. $d^2G_{\max}/dRe^2 < 0$). We explain these behaviors in the following together with other observations.

The present state of superposition of modes $\tilde{\mathbf{q}}$ in Eqs. (25)–(27) can be rewritten as

$$\tilde{E}_1(t) = \tilde{E}_1(0) + (2k^2)^{-1} \sum_{j,k} S_{jk} \int_0^\infty DU_0 (\alpha v_k'^* Dv_j' + \beta \eta_k'^* v_j') dy + \text{c.c.}, \quad (30)$$

$$\tilde{E}_2(t) = \tilde{E}_2(0) - i(2Rek^2)^{-1} \sum_{j,k} S_{jk} \int_0^\infty [\eta_k'^* (k^2 - D^2) \eta_j' + v_k'^* (k^2 - D^2)^2 v_j'] + \text{c.c.}, \quad (31)$$

$$\tilde{E}_3(t) = \tilde{E}_3(0) - id \sum_{j,k} S_{jk} v_k'^*(0) v_j'(0), \quad (32)$$

$$\tilde{E}_4(t) = \tilde{E}_4(0) + i(2Re)^{-1} \sum_{j,k} S_{jk} \{3v_k'^*(0) Dv_j'(0) - k^{-2} v_k'^*(0) D^3 v_j'(0)\} + \text{c.c.}, \quad (33)$$

where $S_{jk} = \kappa_k^* \kappa_j \{ \exp[-i(\omega_j - \omega_k^*)t] - 1 \} / (\omega_j - \omega_k^*)$, \tilde{E}_1 is the energy from the meanflow, \tilde{E}_2 is the energy loss due to viscous dissipation, \tilde{E}_3 is the energy dissipated by wall-damping and \tilde{E}_4 is the energy transferred to the wall by means of the fluid interaction. The initial values $\{\tilde{E}_j(0)\}_{j=1,\dots,4}$ can be chosen such that the total energy is equal to the unity. Without any loss of generality, we choose $\tilde{E}_j(0) = \{1, 0, 0, 0\}$, as these are additive constants and that the temporal evolution far greater than the initial values.

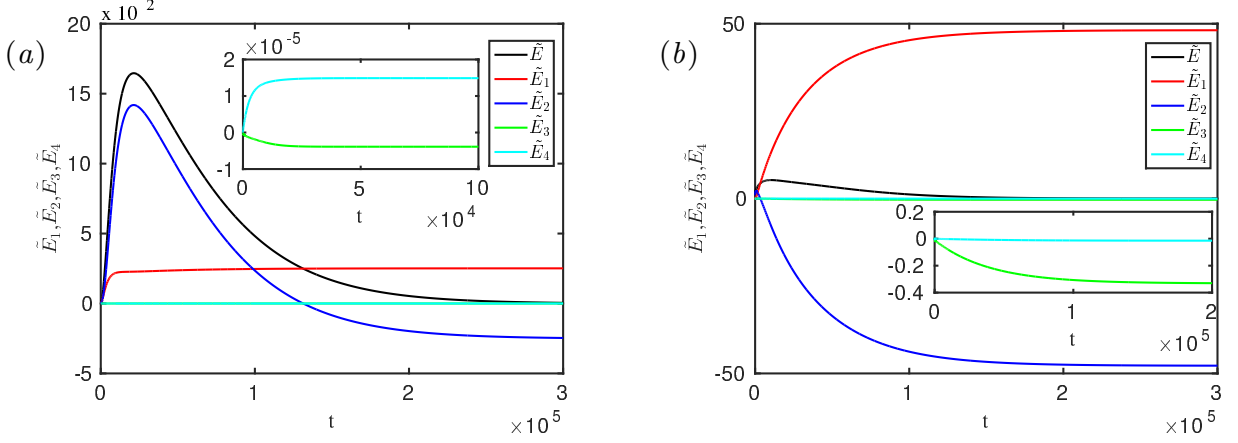


FIG. 13. Transient energy budget for $Re = 1000$, $m = 2$, $d = 1$, $K = 0.3$, $B = 3.2$, $T = 0.75$: (a) $\alpha = 2.5 \times 10^{-4}$, $\beta = 0.09$; (b) $\alpha = 0.002$, $\beta = 0.01$.

Figure 13 shows these components of the total energy for two sets of (α, β) , which are chosen such that they are points in very distinct areas of $G_{\max} = f(\alpha, \beta)$ in Fig. 10(e). First, let us consider the case of vanishing α as in Fig. 13(a). Surprisingly, and unlike the solid-wall case, the viscous dissipation term (\tilde{E}_2) enhances the transient growth in a manner dominant than the mean-shear (\tilde{E}_1). The reason for this finds its origin in the behavior of the eigenfunctions of the continuous spectrum within the boundary layer (see Fig. 2(e)). Specifically, in the region $0 \leq y < 5$, some of these functions—besides having a nonperiodic behavior with respect to y unlike in the freestream—have larger values for higher-order derivatives in comparison to the solid-wall case. In the solid-wall case, though the freestream oscillations are quenched by the mean-shear (shear-sheltering), the values of the higher-order derivatives are small. In the present compliant-wall case, the enhancement in these values due to the specific wall-dynamics results in an increased nonorthogonality. Indeed, the inner-product of the modes with the eigenfunctions in this region could be higher as well. In turn, this contributes to the transient growth. However, as shown in Fig. 13(a), these terms eventually dissipate the energy in the superposition state asymptotically.

However, it is worth noting that the nonsymmetric appearance of α and β in Eqs. (13) & (14) leads to intricate viscosity-dependent effects. Indeed, the actual effects of viscosity depend on the values of (α, β) and how they affect the distribution of the terms D^2v' , D^4v' , $D^2\eta'$. In the situation where (α, β) lie closer to the line of $\beta = 0$ in Fig. 10(e), the predominant transient growth is due to the energy transfer from the meanflow to the superposition-state (see Fig. 13(b)). The reason for this reversed role of the viscous terms on the transient growth will be further discussed later in this section.

Figures 13(a) & 13(b) show that wall-damping effects monotonously remove energy, while the forcing by fluid stress on the wall produces both enhancing as well as adverse effects on the transient growth depending on the values of (α, β) . These results can be understood from the exact solution of the wall equation

$$\tilde{\xi}(t) = \frac{F_2 - \lambda_2 F_1}{\lambda_1 - \lambda_2} e^{\lambda_1 t} + \frac{\lambda_1 F_1 - F_2}{\lambda_1 - \lambda_2} e^{\lambda_2 t} + \sum_j \frac{\kappa_j \sigma'_{22,j}}{(\lambda_1 + i\omega_j)(\lambda_2 + i\omega_j)} e^{-i\omega_j t}, \quad (34)$$

$$\text{where } F_1 = \sum_j \kappa_j \left[\frac{iv'_j(0)}{\omega_j} - \frac{\sigma'_{22,j}}{(\lambda_1 + i\omega_j)(\lambda_2 + i\omega_j)} \right], \quad F_2 = \sum_j \kappa_j \left[v'_j(0) + i\omega_j \frac{\sigma'_{22,j}}{(\lambda_1 + i\omega_j)(\lambda_2 + i\omega_j)} \right],$$

$$\text{and } \lambda_{1,2} = \frac{1}{2m} \left[-\gamma d \pm \sqrt{(\gamma d)^2 - 4m\gamma C(k, \gamma)} \right]. \quad (35)$$

Note that this solution satisfies the initial conditions $\tilde{\xi}(0) = i \sum_j \kappa_j v'_j(0) / \omega_j$ and $\tilde{\xi}_t(0) = \sum_j \kappa_j v'_j(0)$.

In this solution (34), the homogeneous parts (i.e., the first two terms) decay due to the effect of the damping coefficient d . However, the imaginary part of the two exponents λ_1 and λ_2 differ only by a sign, thereby implying

that these two homogeneous parts are orthogonal. This explains the absence of transient growth in the energy lost by the wall-damping in Fig. 13. Furthermore, the solution (34) exhibits transient growth only from the particular solution, which is the response to the forcing by normal stress. As this part of the solution involves summing over the eigenmodes—in which each of them have their own modal temporal evolution—it collectively exhibits transient growth. This explains the presence of transient growth of the energy in Fig. 13(a) due to the term representing forcing by normal stress. Therefore, the root of the transient growth in the displacement of the wall hails from the flow.

Another interesting observation is the fact that when the forcing by the fluid enhances the transient growth of the wall-displacement, so do the viscous effects on the transient growth in flow. Let us recall here that the displacement $\tilde{\xi}$ and velocity $(\tilde{u}, \tilde{v}, \tilde{w})^\top$ are related through the dynamic and kinematic boundary conditions (see Sec. II A), and the continuity equation. A transient growth in $\tilde{\xi}$ due to fluid forcing as per Eq. (34) will result in a transient growth in the velocity field in the layer immediately adjacent to the wall. In turn, this transient growth in that layer of fluid will eventually be transferred to the entire flow domain via viscosity. This results in viscous terms contributing to the growth of the overall disturbance of the combined fluid-wall system. However, when considering the situation where the compliant wall reduces the energy of the system during transients as in the case of Fig. 13(b), the layer of the fluid also loses momentum in order to satisfy the boundary conditions at the wall. In turn, this reduction in the magnitude of the velocity field is spread by viscosity to the entire domain, thereby highlighting the expected and usual dissipative role of viscous terms for such growth (see Fig. 13(a)).

These explanations can also be understood with the help of Eqs. (30)–(33). In these equations, as a matter of convention, let us consider that the dependent variables with complex-conjugate receives the energy from each term where they appear. In the case of $\alpha \approx 0$, we can safely assume that the energy is initially in $v'(y)$ and $w'(y)$ of fluid, as the streaks has not yet formed. The forcing term,

$$T_1 = i(2Re)^{-1} \sum_{j,k} S_{jk} [3v_k'^*(0)Dv_j'(0) - k^{-2}v_k'^*(0)D^3v_j'(0)] + c.c.$$

transfers energy into v' , which is being lost in part by the following damping term

$$T_2 = -id \sum_{j,k} S_{jk} v_k'^*(0)v_j'(0) + c.c..$$

As the wall is being driven, the energy transferred into $v'(0)$ by the forcing can be transferred to $v'(y)$ for $y > 0$ by the following part of the viscous dissipation term

$$T_3 = -i(2Rek^2)^{-1} \sum_{j,k} S_{jk} \int_0^\infty [v_k'^*(k^2 - D^2)^2 v_k'] + c.c.,$$

due to the presence of derivatives. Meanwhile, the mean-shear would transfer the energy from v' into η' through the following term $T_4 = (2k^2)^{-1} \sum_{j,k} S_{jk} \int_0^\infty DU_0 \beta \eta_k'^* v_j' dy + c.c.$, especially near the wall, since DU_0 is maximum at the wall. This transferred energy into $\eta'(y \simeq 0)$ near the wall, gets redistributed to $\eta'(y)$ for y located off the wall by means of the part of the viscous term $T_5 = -i(2Rek^2)^{-1} \sum_{j,k} S_{jk} \int_0^\infty \eta_k'^*(k^2 - D^2)\eta_j' + c.c.$, which is made possible by the presence of the derivatives in the kernel. This detailed picture reveals the dual role played by the viscous terms in the mechanisms of transient growth. In the case of $\beta \sim 0$, the initial and optimal energy is confined to u' and v' . In such situation, the mean-shear transfers the energy from $v'(y \simeq 0)$ close to the wall into u' of the fluid through the term $T_6 = (2k^2)^{-1} \sum_{j,k} S_{jk} \int_0^\infty DU_0 \alpha v_k'^* Dv_j' dy + c.c.$, which is immediately being dissipated by a part of T_3 , namely $T_7 \equiv i(Rek^2)^{-1} \sum_{j,k} S_{jk} \int_0^\infty [v_k'^* D^2 v_k'] + c.c.$

The observation in Fig. 10(d) that the maximum of the transient growth G_{\max} is slower than a linear rate with respect to Re can now be explained based on the above discussion. It is apparent that the viscous terms play a crucial role in the compliant-wall case, in terms of propagating the transient growth from the wall displacement into the flow domain. Therefore, the slower rate of increase for G_{\max} with respect to Re is due to the reduced forcing stress on the compliant wall at high Reynolds number, as is evident from Eq. (12). In the inviscid limit, the transient growth is entirely due to the flow field without any enhancement from the wall dynamics, i.e. the fluid-solid interaction occurs only via one-way coupling as noted before.

Finally, from the solution given by Eq. (34), one can also identify the reason behind the fact that the transient growth is weaker in the solid-wall case in comparison to the compliant-wall one. Indeed, in the limit of $C(k, \gamma) \rightarrow \infty$, the membrane approaches the conditions of a solid wall. In this limit, the norm of the denominator $(\lambda_1 + i\omega_j)(\lambda_2 + i\omega_j)$ in one of the terms in Eq. (34) tends to blow up, thus weakening the response to forcing. Therefore, in the solid-wall limit, the major contribution of the present situation vanishes altogether, and the transient growth is purely limited to the effects associated with the inviscid feature of the flow.

V. CONCLUSIONS

In this paper, the temporal modal and nonmodal growth of three dimensional perturbations in the boundary layer flow over an infinite compliant flat wall has been investigated. The two key findings from this work are the following. First, the flow is found to have an instability mechanism reminiscent of that of a forced and damped harmonic oscillator. We confirmed that the combined system of fluid and compliant wall have stable/unstable modes as predicted by the phase of the forcing and damping terms. Second, in stark contrast to the solid-wall problem, the transient growth in the compliant-wall case involves a nontrivial contribution of viscous terms, in particular for the dynamics of streamwise-independent modes. It is found that this contribution stems from the role of viscous terms in communicating the transient growth from the wall displacement to the fluid, which in turn stems from the nonmodal growth of the forcing by the fluid on the wall.

From the formalism standpoint, we approached this problem using a two-variable formulation—wall-normal velocity and wall-normal vorticity, which significantly simplifies the treatment of boundary conditions. Specifically, with this two-variable formulation the quadratic dependence on the eigenvalue parameter vanishes, thereby drastically reducing the computational effort required to obtain the spectra. Furthermore, we were able to accurately compute the discrete and continuous modes from the two separate systems, thus enabling us to properly filter the pseudospectra so as to obtain highly-accurate eigenfunctions. Still with the help of this two-variable formulation, we determined an instance of each of the hydroelastic modes—static wave divergence, traveling wave flutter and transitional modes, and analyzed the associated eigenfunctions and their stability through an energy budget analysis. In addition, we identified the instability regions in the parameters space and also analyzed the growth rate of hydroelastic and Tollmien–Schlichting modes. For all cases considered, our approach allowed us to obtain accurate continuous spectra for large negative values of c_i . It is important to highlight that having access to clean continuous spectra without the pseudospectra is an essential prerequisite to performing the transient growth study.

This boundary layer flow over an infinite compliant wall exhibits a higher transient growth, though at a slower rate, as compared to the same flow over a solid wall. In the solid-wall case, the maximum growth rate for streamwise independent modes scales according to $G_{\max} \sim \mathcal{O}(Re^2)$. Here, in the compliant-wall case, this scaling law breaks down as a consequence of the nontrivial dependence of the wall-boundary conditions on the Reynolds number. The maximum of the transient growth, G_{\max} , increases with Re at a sublinear pace. Using a nonmodal energy budget analysis, this fact was found to be due to a reduced forcing at higher Re , which in turn reduces the above-mentioned viscous effects on the transient growth. Other results were found to be similar to those observed in the solid-wall case. For instance, the superposition of streamwise independent modes have a stronger transient growth as compared to the modes with $\alpha > 0$.

With soft compliant walls, the transient growth is enhanced since there is a more intense response of the wall to the forcing of the fluid. The analytical solution to the equation governing the dynamics of the wall allowed us to exactly identify the root cause of this effect.

Lastly, the initial and optimal patterns of the 2D modes were found not to exhibit the phenomenon associated with the Orr-mechanism where velocity fluctuations appear to counter the effect of the mean-shear initially, and the rotation of these vortical structures end up being aligned with the mean-shear at the optimal time. This phenomenon is related to the nonconservation of circulation because of the time-dependent influx of vorticity generated by the wall dynamics. Nonetheless, the initial and optimal patterns of the velocity field are similar to those in the solid-wall case, except that the wall deformation provides a storage of potential energy at the optimal time.

-
- [1] P. W. Carpenter, C. Davies, and A. D. Lucey, “Hydrodynamics and compliant walls: Does the dolphin have a secret,” *Curr. Sci.* **79**, 758–765 (2000).
 - [2] J. B. Grotberg and O. E. Jensen, “Biofluid mechanics in flexible tubes,” *Annu. Rev. Fluid Mech.* **36**, 121 (2004).
 - [3] M. O. Kramer, “Boundary-layer stabilization by distributed damping,” (1957).
 - [4] K.-H. Chung, *Composite compliant coatings for drag reduction utilizing low modulus high damping silicone rubber*, Ph.D. thesis, Massachusetts Institute of Technology (1985).
 - [5] P. W. Carpenter and A. D. Garrad, “The hydrodynamic stability of flow over Kramer-type compliant surfaces. Part 1. Tollmien–Schlichting instabilities,” *J. Fluid Mech.* **155**, 465–510 (1985).
 - [6] C. Davies and P. W. Carpenter, “Numerical simulation of the evolution of Tollmien–Schlichting waves over finite compliant panels,” *J. Fluid Mech.* **335**, 361–392 (1997).
 - [7] M. Gaster, “Is the dolphin a red herring?” in *Turbulence management and relaminarisation* (Springer, 1988) pp. 285–304.
 - [8] M. T. Landahl, “On the stability of a laminar incompressible boundary layer over a flexible surface,” *J. Fluid Mech.* **13**, 609–632 (1962).
 - [9] A. Kornecki, “Aeroelastic and hydroelastic instabilities of infinitely long plates. I,” *Solid Mech. Arch.* **3**, 381–440 (1978).

- [10] A. E. Dixon, A. D. Lucey, and P. W. Carpenter, "Optimization of viscoelastic compliant walls for transition delay," *AIAA J.* **32**, 256–267 (1994).
- [11] M. Gad-El-Hak, R. F. Blackwelder, and J. J. Riley, "On the interaction of compliant coatings with boundary-layer flows," *J. Fluid Mech.* **140**, 257–280 (1984).
- [12] P. W. Carpenter and A. D. Garrad, "The hydrodynamic stability of flow over Kramer-type compliant surfaces. Part 2. Flow-induced surface instabilities," *J. Fluid Mech.* **170**, 199–232 (1986).
- [13] P. K. Sen and D. S. Arora, "On the stability of laminar boundary-layer flow over a flat plate with a compliant surface," *J. Fluid Mech.* **197**, 201–240 (1988).
- [14] M. Gad-el Hak, "Compliant coatings: a decade of progress," *Appl. Mech. Rev.* **49**, S147–S157 (1996).
- [15] C. Davies, "Convective and absolute instabilities of flow over compliant walls," in *Flow past highly compliant boundaries and in collapsible tubes* (Springer, 2003) pp. 69–93.
- [16] O. Wiplier and U. Ehrenstein, "On the absolute instability in a boundary-layer flow with compliant coatings," *Eur. J. Mech.-B/Fluid.* **20**, 127–144 (2001).
- [17] P. W. Carpenter, "Optimization of multiple-panel compliant walls for delay of laminar-turbulent transition," *AIAA J.* **31**, 1187–1188 (1993).
- [18] K. Tsigklifis and A. D. Lucey, "Global instabilities and transient growth in Blasius boundary-layer flow over a compliant panel," *Sadhana* **40**, 945–960 (2015).
- [19] K. S. Yeo, B. C. Khoo, and H. Z. Zhao, "The absolute instability of boundary-layer flow over viscoelastic walls," *Theor. Comp. Fluid Dyn.* **8**, 237–252 (1996).
- [20] J. Hoepffner, A. Bottaro, and J. Favier, "Mechanisms of non-modal energy amplification in channel flow between compliant walls," *J. Fluid Mech.* **642**, 489–507 (2010).
- [21] K. M. Butler and B. F. Farrell, "Three-dimensional optimal perturbations in viscous shear flow," *Phys. Fluids A: Fluid* **4**, 1637–1650 (1992).
- [22] L. N. Trefethen, A. Trefethen, S. C. Reddy, T. Driscoll, *et al.*, "Hydrodynamic stability without eigenvalues," *Science* **261**, 578–584 (1993).
- [23] P. J. Schmid and D. S. Henningson, *Stability and Transition in Shear Flows*, Vol. 142 (Springer Science & Business Media, 2001).
- [24] C. E. Grosch and H. Salwen, "The continuous spectrum of the Orr–Sommerfeld equation. Part 1. the spectrum and the eigenfunctions," *J. Fluid Mech.* **87**, 33–54 (1978).
- [25] G. H. Golub and C. F. Van Loan, *Matrix Computations*, 4th ed. (The Johns Hopkins University Press, Baltimore, MD, 2013).
- [26] Matlab `bvp5c`, which has the limitation that it can only give one eigenvalue and the corresponding eigenfunction.
- [27] L. N. Trefethen and M. Embree, *Spectra and pseudospectra: the behavior of nonnormal matrices and operators* (Princeton University Press, 2005).
- [28] R. G. Jacobs and P. A. Durbin, "Shear sheltering and the continuous spectrum of the Orr–Sommerfeld equation," *Phys. Fluids* **10**, 2006–2011 (1998).
- [29] P. G. Drazin and L. N. Howard, "The instability to long waves of unbounded parallel inviscid flow," *J. Fluid Mech.* **14**, 257–283 (1962).
- [30] P. S. Stewart, S. L. Waters, and O. E. Jensen, "Local instabilities of flow in a flexible channel: asymmetric flutter driven by a weak critical layer," *Phys. Fluids* **22**, 031902 (2010).
- [31] P. W. Carpenter, "Status of transition delay using compliant walls," in *Viscous drag reduction in boundary layers*, Vol. 123, edited by D. M. Bushnell and J. N. Hefner (AIAA, 1990) pp. 79–113.
- [32] T. B. Benjamin, "The threefold classification of unstable disturbances in flexible surfaces bounding inviscid flows," *J. Fluid Mech.* **16**, 436–450 (1963).
- [33] L. H. Gustavsson, "Energy growth of three-dimensional disturbances in plane poiseuille flow," *J. Fluid Mech.* **224**, 241–260 (1991).
- [34] G. Kreiss, A. Lundbladh, and D. S. Henningson, "Bounds for threshold amplitudes in subcritical shear flows," *J. Fluid Mech.* **270**, 175–198 (1994).
- [35] P. J. Schmid, "Linear stability theory and bypass transition in shear flows," *Phys. Plasmas* **7**, 1788–1794 (2000).
- [36] M. Malik, J. Dey, and M. Alam, "Linear stability, transient energy growth, and the role of viscosity stratification in compressible plane couette flow," *Phys. Rev. E* **77**, 036322 (2008).